

pubs.acs.org/JPCC Article

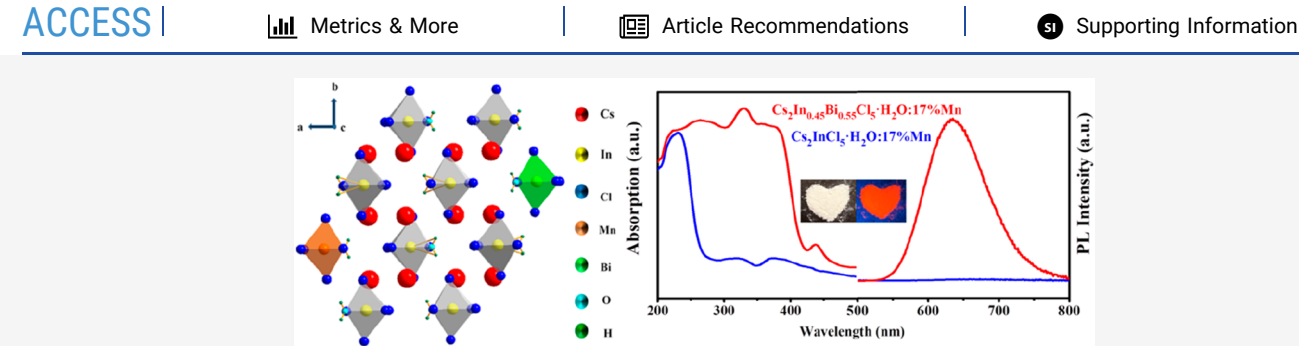
# Enhancing Photoluminescence and Stability of Mn-Doped Cs<sub>2</sub>InCl<sub>5</sub>·H<sub>2</sub>O Microcrystals with Introduced Bi<sup>3+</sup> Ion

Liang Jing, Qingmei Cen, Qi Pang,\* and Jin Zhong Zhang

**(** 

Cite This: J. Phys. Chem. C 2023, 127, 2448-2455





**ABSTRACT:** In this work, lead-free zero-dimensional (0D) all-inorganic perovskite  $Mn^{2+}$ -doped  $Cs_2InCl_5 \cdot H_2O$  microcrystals (MCs) with introduced  $Bi^{3+}$  ion were synthesized by supersaturation recrystallization at room temperature. The electronic bandgap of the MCs is tuned from ~5.1 to ~3.1 eV, and the electronic absorption is enhanced in the 200–400 nm region by  $Bi^{3+}$  incorporation. Upon excitation at 365 nm, the MCs with introduced  $Bi^{3+}$  exhibit strong red emission peaking at 640 nm, which is attributed to the  $Mn^{2+}$  transition ( ${}^4T_{1g} \rightarrow {}^6A_{1g}$ ). Simultaneous  $Mn^{2+}$  and  $Bi^{3+}$  incorporation into  $Cs_2InCl_5 \cdot H_2O$  shows 60 times enhancement of the 640 nm emission band compared to  $Mn^{2+}$  alone. This PL enhancement is attributed to the energy transfer (ET) from the  $[BiCl_6]^{3-}$  octahedron, which acts as a UV light absorber and exciton donor, to  $[MnCl_6]^{4-}$ . In addition, a yellow-light-emitting diode (LED) device based on the  $Cs_2In_{0.45}Bi_{0.55}Cl_5 \cdot H_2O \cdot 17\%Mn$  MCs was fabricated and evaluated, showing high color saturation at a drive current of 420 mA and good stability. This study demonstrates a new method for achieving efficient red emission by incorporating  $ns^2$  metal ions and Mn ions in 0D lead-free metal halides.

## ■ INTRODUCTION

All-inorganic lead halide perovskites have attracted substantial attention due to their unique properties and potential applications. 1-5 However, their toxicity (with Pb) and instability under ambient conditions limit their applications and have generated strong interest in developing nontoxic and stable alternatives.<sup>6-9</sup> Low-dimensional lead-free luminescent metal halides with a unique soft lattice have aroused reviving interest due to their outstanding optical properties including a large absorption coefficient, high photoluminescence quantum yield (PLQY), broad emission band, and large Stokes shift. 10-16 These advantages make them ideal candidates as a new class of luminescent materials and as an alternative to lead halide perovskites. Among these, zero-dimensional (0D) Inbased metal halides, such as  $A_3InX_6$  (A = Cs and Rb), <sup>17,18</sup> have become the focus of attention owing to their spatially and electronically decoupled 0D structure that favors strongly localized excitonic states. <sup>19–24</sup> Specifically, through the control of the A cation and the octahedral unit, highly efficient and largely Stokes-shifted visible luminescence, stemming from self-trapped exciton (STE) states, was achieved in 5s<sup>2</sup> metal Sb<sup>3+</sup>- or Te<sup>4+</sup>-doped 0D In-based halide crystals. For example, in 2020, Xia et al. discovered a novel all-inorganic lead-free Cs<sub>2</sub>InCl<sub>5</sub>·H<sub>2</sub>O single crystal (SC), and a broadband yellow

emission with a high PLQY of 95.5% by doping  $Sb^{3+}$  has been achieved. Es Kuang et al. reported an all-inorganic  $Te^{4+}$ -doped  $Cs_2InCl_5\cdot H_2O$  SC with bright orange emission, which shows the significant potential of these materials for application in wearable and portable thermometry devices. In 2022, Chen et al. systematically investigated 0D  $Sb^{3+}$ -doped  $Cs_3InCl_6$  luminescent NCs from the controlled synthesis and fundamental photophysics to the phase transformation. In addition, Han et al. reported that  $(Rb_xCs_{1-x})_3InCl_6$  shows green emission with a microsecond long lifetime.

Manganese ( $Mn^{2+}$ ) is widely used as a suitable dopant in doping technology. The  $Mn^{2+}$  octahedron usually exhibits orange emission due to the  ${}^4T_{1g} \rightarrow {}^6A_{1g}$  transition and magnetic properties and is insensitive to the physical and electronic structure of the host.  ${}^{27-30}$  For example, it has been demonstrated that  $Mn^{2+}$ -doped lead-based, copper-based,

Received: November 30, 2022 Revised: January 18, 2023 Published: January 27, 2023





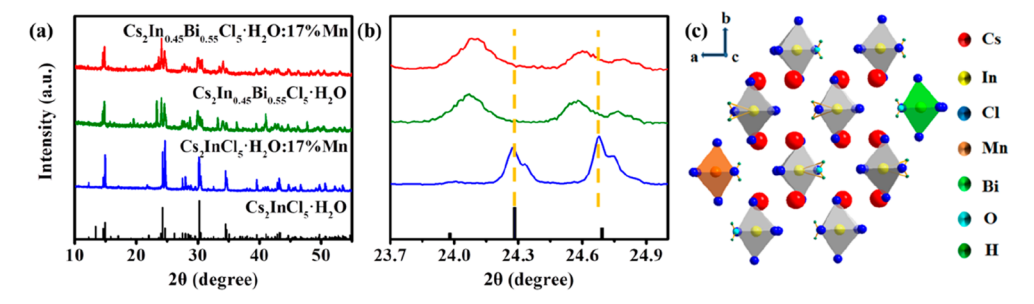


Figure 1. (a) XRD patterns of pristine  $Cs_2InCl_5 \cdot H_2O$ ,  $Cs_2InCl_5 \cdot H_2O \cdot 17\%Mn$ ,  $Cs_2In_{0.45}Bi_{0.55}Cl_5 \cdot H_2O$ , and  $Cs_2In_{0.45}Bi_{0.55}Cl_5 \cdot H_2O \cdot 17\%Mn$ . (b) Magnification of the XRD patterns in the  $23.7^{\circ}-25.0^{\circ}$  range. (c) Illustration of the crystal structure of  $Mn^{2+}$ -doped and  $Bi^{3+}$ -alloyed  $Cs_2InCl_5 \cdot H_2O$ .

bismuth-based, antimony-based, and other metal halide perovskites exhibit outstanding photoelectric properties. 31–36 Despite these encouraging results, Mn<sup>2+</sup> doping in 0D In-based halide crystals is still largely unexplored. Therefore, it is worthwhile to explore and significantly incorporate Mn<sup>2+</sup> into the 0D In-based halide to improve the photoelectric performance. Furthermore, most 0D In-based halides are synthesized by using complex procedures at high reaction temperatures, and their excitation energies are too high (<350 nm), both of which are issues that must be addressed.

In this work, a series of novel Mn-doped Cs<sub>2</sub>InCl<sub>5</sub>·H<sub>2</sub>O microcrystals (MCs) with introduced Bi3+ ions were prepared using room-temperature supersaturation recrystallization. The crystal structures of pristine and Mn<sup>2+</sup>/Bi<sup>3+</sup>-incorporated Cs<sub>2</sub>InCl<sub>5</sub>·H<sub>2</sub>O MCs was determined by X-ray diffraction (XRD) while the morphology was characterized by scanning electron microscopy (SEM). X-ray photoelectron spectroscopy (XPS) was used to characterize the electronic structures. Their optical properties and dynamic properties were studied using temperature-dependent steady-state and time-resolved PL spectroscopy. The Mn<sup>2+</sup>-doped MCs with introduced Bi<sup>3+</sup> ion exhibit a strong PL band peaked at 640 nm assigned to the 3d<sup>5</sup> Mn<sup>2+</sup> transition ( ${}^4T_{1g} \rightarrow {}^6A_{1g}$ ) upon excitation with 365 nm light. The introduction of Bi<sup>3+</sup> significantly enhances the Mn<sup>2+</sup> emission. Furthermore, the Mn<sup>2+</sup>-doped and Bi<sup>3+</sup>alloyed Cs2InCl5·H2O MCs show good stability and demonstrate good potential for LED application.

## METHODS

**Chemicals.** Cesium chloride (CsCl, 99.9%, Aladdin), indium(III) chloride (InCl<sub>3</sub>, 99%, Aladdin), bismuth(III) chloride (BiCl<sub>3</sub>, 99.9%, Aladdin), manganese chloride tetrahydrate (MnCl<sub>2</sub>·4H<sub>2</sub>O, 99.99%, Aladdin), hydrochloric acid (HCl, 36.0%—38.0%, KESHI), and isopropyl alcohol (IPA, 99.7%, GHTECH) were used as purchased without any further purification.

**Synthesis.** The Cs<sub>2</sub>InCl<sub>5</sub>·H<sub>2</sub>O metal halides were easily synthesized by the vigorous stirring of InCl<sub>3</sub> (0.4 mmol) precursor in hydrochloric acid at room temperature. Then CsCl (0.8 mmol) was added to the reaction mixture, which immediately led to the precipitation of microcrystals. The reaction was continued for another 3.0 h to make sure that it is complete. The precipitates were washed with isopropanol and centrifuged at 8000 rpm two times. The powders were then dried at 50 °C for 2.0 h and then stored in a glass vial under ambient conditions for further characterization.

The synthesis procedure of the  $Cs_2InCl_5 \cdot H_2O \cdot Mn$  method is very much similar to that for the  $Cs_2InCl_5 \cdot H_2O$  discussed above, except for adding appropriate amounts of  $MnCl_2 \cdot 4H_2O$ 

to the reaction mixture in hydrochloric acid. The optimum value of  $MnCl_2\cdot 4H_2O$  was found to be 0.08 mmol (the molar feed ratio of Mn/(Mn+In) is 17%), for which the best PL properties were obtained. Therefore, we finalized this composition when synthesizing different amounts of Bi alloyed  $Cs_2InCl_5\cdot H_2O$ : Mn, and the samples were noted as  $Cs_2In_{1-x}Bi_xCl_5\cdot H_2O$ :17%Mn. The different amounts of BiCl<sub>3</sub> (fed at x=0, 0.20, 0.40, and 0.55) were 0, 0.08, 0.16, and 0.22 mmol, respectively. The synthesis method of  $Cs_2In_{1-x}Bi_xCl_5\cdot H_2O$ :17%Mn. Similarly,  $Pb^{2+}$ - or  $Sb^{3+}$ -alloyed  $Cs_2InCl_5\cdot H_2O$ :17%Mn were obtained.

Characterization. X-ray diffraction (XRD) measurements of the perovskite powders were performed on a SMAR-TLAB3KW powder diffractometer using a Cu K $\alpha$  radiation source with operating voltage parameters of 40 kV and 30 mA. The UV-vis diffuse reflectance spectra of the solid powder were measured with a Techcomp UV2600 variable slit UV-vis spectrophotometer. Spectral characterizations were obtained with a FLS1000 fluorescence spectrometer from Edinburgh Instruments. In addition to temperature-dependent PL, PL and PLE were measured at room temperature using xenon (Xe900) as the excitation source. Time-resolved PL (TRPL) is measured with an excitation source microsecond lamp. PLQY is an Edinburgh Instruments integrating sphere using a FLS-1000 fluorescence spectrometer and PMT-900 detector to record absolute PLQY measurements. Electron paramagnetic resonance (EPR) spectra were acquired at room temperature in the X-band of a Bruker-A300-10/12 spectrometer. The morphology and size of the sample powders were characterized by scanning electron microscopy (SEM). The elemental composition and distribution of the material were observed by energy-dispersive X-ray spectroscopy (EDS) coupled with an SEM. X-ray photoelectron spectroscopy (XPS) was performed using a Thermal Fisher ESCALAB 250XI spectrometer.

## RESULTS AND DISCUSSION

Pristine  $Cs_2InCl_5\cdot H_2O$  and  $Cs_2InCl_5\cdot H_2O:17\%Mn$  MCs were synthesized via a mild one-step solution method in hydrochloric acid at room temperature. We introduced different amounts of BiCl<sub>3</sub> to the precursor solution of  $In^{3+}$  and  $Mn^{2+}$  ions with the molar ratio of Bi to (In + Bi) set to 0, 0.20, 0.40, and 0.55. A schematic illustration of the formation of the  $Cs_2In_{1-x}Bi_xCl_5\cdot H_2O:17\%Mn$  is shown in Figure S1a. The XRD patterns of the pristine  $Cs_2InCl_5\cdot H_2O$ ,  $Cs_2InCl_5\cdot H_2O:17\%Mn$ ,  $Cs_2In_{0.45}Bi_{0.55}Cl_5\cdot H_2O$ , and  $Cs_2In_{0.45}Bi_{0.55}Cl_5\cdot H_2O:17\%Mn$  are shown in Figure 1a. All samples possess orthorhombic phase structures of  $Cs_2InCl_5\cdot H_2O$ , indicating the appropriate  $Mn^{2+}$ 

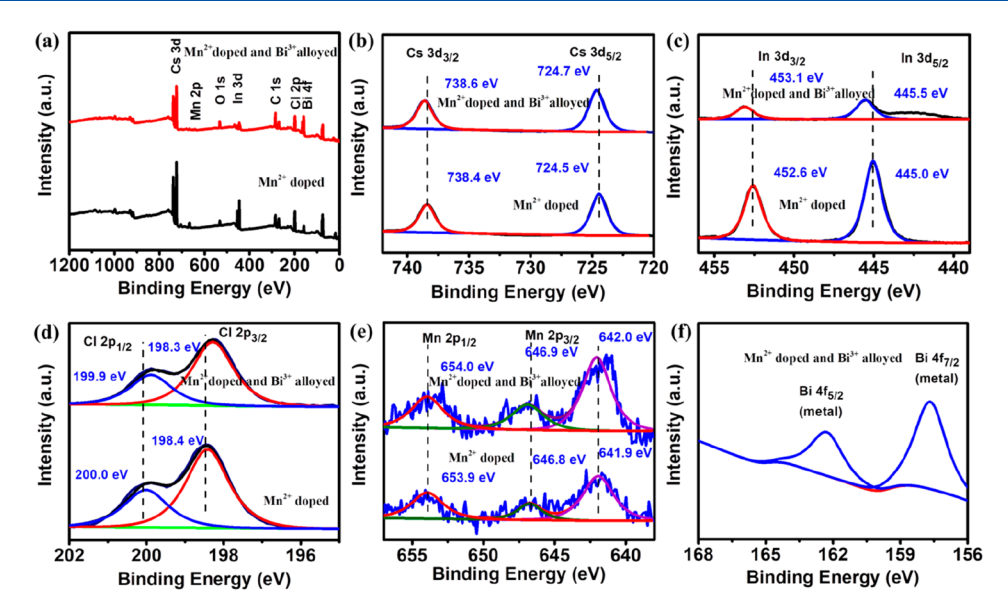


Figure 2. (a) XPS survey spectra and high-resolution XPS spectra of (b) Cs 3d, (c) In 3d, (d) Cl 2p, (e) Mn 2p, and (f) Bi 4f of Mn<sup>2+</sup>-doped and Bi<sup>3+</sup>-alloyed Cs<sub>2</sub>InCl<sub>5</sub>·H<sub>2</sub>O MCs.

doping or Bi<sup>3+</sup> alloying does not change the crystalline phase. A set of characteristic peaks in the  $2\theta$  region of  $23.7^{\circ}-25^{\circ}$  can be assigned to the (002) and (221) crystal planes (Figure 1b). There is no significant shift in the angles of Cs<sub>2</sub>InCl<sub>5</sub>·H<sub>2</sub>O and  $Cs_2InCl_5 \cdot H_2O:17\%Mn$  as  $In^{3+}$  and  $\widetilde{M}n^{2+}$  have a comparable ionic radius. The diffraction peaks of Cs<sub>2</sub>In<sub>0.45</sub>Bi<sub>0.55</sub>Cl<sub>5</sub>·H<sub>2</sub>O shift to lower angles compared to that of Cs<sub>2</sub>InCl<sub>5</sub>·H<sub>2</sub>O owing to the larger ions radius of Bi3+ than In3+, causing lattice expansion. Similarly, the diffraction peaks of Bi<sup>3+</sup> alloyed Cs<sub>2</sub>InCl<sub>5</sub>·H<sub>2</sub>O:17%Mn shift to a lower angle. However, with more  $Bi^{3+}$  incorporated (fed at y = 0.60), a one-dimensional (1D) Cs<sub>3</sub>Bi<sub>2</sub>Cl<sub>9</sub> orthorhombic phase is formed. Extra impurities can be observed at 33.6°, 41.5°, and 48.4° which are assigned to the diffraction of Cs<sub>3</sub>Bi<sub>2</sub>Cl<sub>9</sub>, as shown in Figure S1b. Therefore, we determined  $Bi^{3+}$  fed at y = 0.55 as the optimal alloying amount for the following discussion. The pure Cs<sub>2</sub>InCl<sub>5</sub>·H<sub>2</sub>O phase was confirmed by XRD analysis with the space group *Pnma* (Figure 1c). In this structure, each In<sup>3+</sup> ion is coordinated with five Cl ions and one O2 ion from the coordinating water, forming a structural unit of [InCl<sub>5</sub>H<sub>2</sub>O]<sup>2-</sup> octahedron. The  $[InCl_5H_2O]^{2-}$  octahedrons are isolated from each other and separated by two Cs+ cations to form a 0D structure.

Figure S2a,b shows the SEM images of the  $Cs_2InCl_5$ · $H_2O:17\%Mn$  and  $Cs_2In_{0.45}Bi_{0.55}Cl_5\cdot H_2O:17\%Mn$ . The SEM images of both samples show microsize particles. The EDS spectra were measured to determine the elemental composition of  $Cs_2In_{0.45}Bi_{0.55}Cl_5\cdot H_2O:17\%Mn$ . In Figure S2c—h, elements of Cs, In, Cl, Mn, and Bi are found in the EDS spectrum, indicating both  $Mn^{2+}$  and  $Bi^{3+}$  are successfully doped or alloyed.

The actual doping content of  $Mn^{2+}$  and  $Bi^{3+}$  in different amounts of  $Bi^{3+}$  alloyed samples was determined by ICP-OES, and the results are shown in Table S1. With the increase of  $Bi^{3+}$  content, ICP results showed that the  $Bi^{3+}$  content also increased, while the  $Mn^{2+}$  content remained almost constant. In the  $Cs_2In_{0.45}Bi_{0.55}Cl_5\cdot H_2O:17\%Mn$  sample, the actual alloying level of  $In^{3+}$  was estimated to be 52.09%, while the actual amounts of  $Mn^{2+}$  and  $Bi^{3+}$  were 10.45% and 37.45%. Therefore, it can be seen that  $Mn^{2+}$  is slightly doped while  $Bi^{3+}$ 

is alloyed to  $Cs_2InCl_5 \cdot H_2O$ . The results are consistent with the indium-based phase shown by XRD. In the following, we use the feed molar ratio for discussion.

To determine the elemental composition and electronic properties of Cs<sub>2</sub>In<sub>0.45</sub>Bi<sub>0.55</sub>Cl<sub>5</sub>·H<sub>2</sub>O:17Mn, XPS was conducted to investigate the surface chemical environment of Cs<sub>2</sub>InCl<sub>5</sub>·H<sub>2</sub>O:17%Mn and Cs<sub>2</sub>In<sub>0.45</sub>Bi<sub>0.55</sub>Cl<sub>5</sub>·H<sub>2</sub>O:17%Mn (Figure 2a-f). As shown in Figure 2a, both samples exhibit characteristic peaks correlated to Cs, In, Mn, Cl, C, and O elements and add Bi in the Bi alloying samples. In Figure 2b, after Bi3+ alloyed, two Cs 3d peaks at 738.4 and 724.5 eV corresponding to Cs 3d<sub>3/2</sub> and Cs 3d<sub>5/2</sub> both move 0.2 eV toward higher binding energy achieving 738.6 and 724.7 eV. As shown in Figure 2c, the In<sup>3+</sup> 3d spectra of Cs<sub>2</sub>InCl<sub>5</sub>·H<sub>2</sub>O have two characteristic peaks: In  $3d_{3/2}$  and  $3d_{5/2}$  at 452.6 and 445.0 eV, respectively. With the Bi<sup>3+</sup> alloyed, the binding energies of In  $3d_{3/2}$  and  $3d_{5/2}$  move to a higher energy with 0.5 eV, resulting in a reduction in the overlap of the electron cloud. The Mn  $2p_{1/2}$  and Mn  $2p_{3/2}$  peaks also have a weak shift of 0.1 eV to a higher binding energy at 653.9 and 641.9 eV. The peaks of Cs 3d, Mn 2p, and In<sup>3+</sup> 3d all move toward higher binding energy corresponding to the unalloyed sample due to Bi<sup>3+</sup> incorporating, in which the lattice expands when Bi<sup>3+</sup> with a larger ionic radius replaces In<sup>3+</sup> ions and results in electron density reducing around these ions. Meanwhile, the electronegativity of Bi is larger than those of Mn, Cs, and In, which leads to Cs, In, and Mn moving to high binding energies. In Figure 2d, Cl<sup>-</sup> is shifted 0.1 eV to lower binding energy due to Cl<sup>-</sup> having the largest electronegativity. As shown in Figure 2f, two peaks appear at 162.2 and 157.6 eV, further indicating that Bi<sup>3+</sup> was successfully incorporated.

Electron paramagnetic resonance (EPR) experiments were conducted to investigate the magnetic property of  $\mathrm{Mn^{2+}}$ -doped  $\mathrm{Cs_2InCl_5}\cdot\mathrm{H_2O}$ . Figure 3 shows the X-band electron paramagnetic resonance (EPR) spectra of  $\mathrm{Bi^{3+}}$ -alloyed and unalloyed samples at room temperature. Both of the graphs show the 6-fold hyperfine split structure caused by the spin (S = 5/2) and nuclear spin (I = 5/2) of the unpaired  $\mathrm{3d^5}$  electron of the  $\mathrm{Mn^{2+}}$  ion, which provides direct experimental access to the alignment ordering of the  $\mathrm{Mn^{2+}}$  spins and to the presence

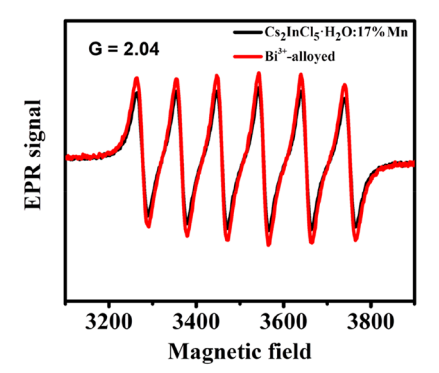


Figure 3. X-band EPR spectra of Cs<sub>2</sub>InCl<sub>5</sub>·H<sub>2</sub>O:17%Mn and Bi<sup>3+</sup>-alloyed Cs<sub>2</sub>InCl<sub>5</sub>·H<sub>2</sub>O:17%Mn MCs.

of magnetic coupling effects that are indicative of interdopant interactions and confirms that  $\mathrm{Mn^{2+}}$  ions are successfully doped and the  $\mathrm{Bi^{3+}}$  alloying had little effect on the  $\mathrm{Mn^{2+}}$  ion. The external test obtained G=2.04, which was similar to a previous report.<sup>37</sup>

The influence of Mn doping on the optical properties and band structures of the Bi<sup>3+</sup>-alloyed Cs<sub>2</sub>InCl<sub>5</sub>·H<sub>2</sub>O was studied using UV–vis absorption and PL spectroscopy. As shown in Figure 4a, the pristine Cs<sub>2</sub>InCl<sub>5</sub>·H<sub>2</sub>O and Cs<sub>2</sub>InCl<sub>5</sub>·H<sub>2</sub>O:17% Mn show an abrupt absorption edge at 250 nm. This is similar to the reported absorption spectra of 0D Cs<sub>2</sub>InCl<sub>5</sub>·H<sub>2</sub>O NCs, and the very weak absorption at 350 nm is ascribed to the parity transition of In<sup>3+,25</sup> While, through Bi<sup>3+</sup> alloying, a higher absorption is located at 250–400 nm with two absorption humps at about 330 and 376 nm, which are assigned to the transitions of octahedral [BiX<sub>6</sub>]<sup>3-</sup> from the 6s<sup>2</sup>-6s<sup>1</sup>p<sup>1,38-40</sup> The absorption edge of Cs<sub>2</sub>InCl<sub>5</sub>·H<sub>2</sub>O red-

shifts from ~260 to ~420 nm, which indicates that the bandgap would be reduced by Bi3+ alloying. Two distinct absorption peaks at 438 and 535 nm in Cs<sub>2</sub>In<sub>0.45</sub>Bi<sub>0.55</sub>Cl<sub>5</sub>· H<sub>2</sub>O:17%Mn are assigned to the characteristic absorption peaks of the Mn<sup>2+</sup> transition from <sup>6</sup>A<sub>1g</sub> to <sup>4</sup>T<sub>1g</sub>. Therefore, the enhanced UV light harvesting for Cs<sub>2</sub>In<sub>0.45</sub>Bi<sub>0.55</sub>Cl<sub>5</sub>·H<sub>2</sub>O:17% Mn compared with Cs<sub>2</sub>InCl<sub>5</sub>·H<sub>2</sub>O:17%Mn is contributed to the introduced  $[BiX_6]^{3-}$  octahedrons. To determine the nature of the bandgap  $(E_g)$ , we then analyzed the Tauc plot of the diffuse reflectance spectrum of Cs<sub>2</sub>InCl<sub>5</sub>·H<sub>2</sub>O:17%Mn and Cs<sub>2</sub>In<sub>0.45</sub>Bi<sub>0.55</sub>Cl<sub>5</sub>·H<sub>2</sub>O:17%Mn (Figure 4b). By setting the exponential factor to 2, all directly allowed transition characteristics of Cs2InCl5·H2O:17%Mn and Cs<sub>2</sub>In<sub>0.45</sub>Bi<sub>0.55</sub>Cl<sub>5</sub>·H<sub>2</sub>O:17%Mn can be well fitted. The fitting results show that the electronic bandgap can be dramatically tuned from ~5.1 to ~3.1 eV by Bi3+ alloying, indicating that the Bi<sup>3+</sup> alloying allowed us to tune the absorption band edge of Cs<sub>2</sub>InCl<sub>5</sub>·H<sub>2</sub>O.

The PL spectra of the pristine  $Cs_2InCl_5 \cdot H_2O$ ,  $Cs_2InCl_5 \cdot H_2O:17\%Mn$ ,  $Cs_2In_{0.45}Bi_{0.55}Cl_5 \cdot H_2O$ , and  $Cs_2In_{0.45}Bi_{0.55}Cl_5 \cdot H_2O:17\%Mn$  are shown in Figure 4c. The pristine sample and  $Cs_2InCl_5 \cdot H_2O:17\%Mn$  show a weak PL when excited at 250 nm. However, they were nonluminous upon excitation at 365 nm. The  $Cs_2In_{0.45}Bi_{0.55}Cl_5 \cdot H_2O$  also shows no PL excited at 365 nm. Interestingly, upon alloying  $Bi^{3+}$  into  $Cs_2InCl_5 \cdot H_2O:17\%Mn$ , the sample exhibits strong red emission centered at  $\sim$ 640 nm with a PLQY of 1.82% and full width at half-maximum (FWHM) of  $\sim$ 80 nm, which is ascribed to the parity and spin-forbidden  $^4T_{1g}$  (G)  $\rightarrow$   $^6A_{1g}$  (S) transition of octahedral coordinated  $Mn^{2+}$  ions rather than the broadband STEs emission. Therefore, it is reasonable to assume that in the system of  $Cs_2InCl_5 \cdot H_2O$  MCs cobound by  $ns^2$  metal ions and  $Mn^{2+}$ , the luminescence of STE is inhibited due to the

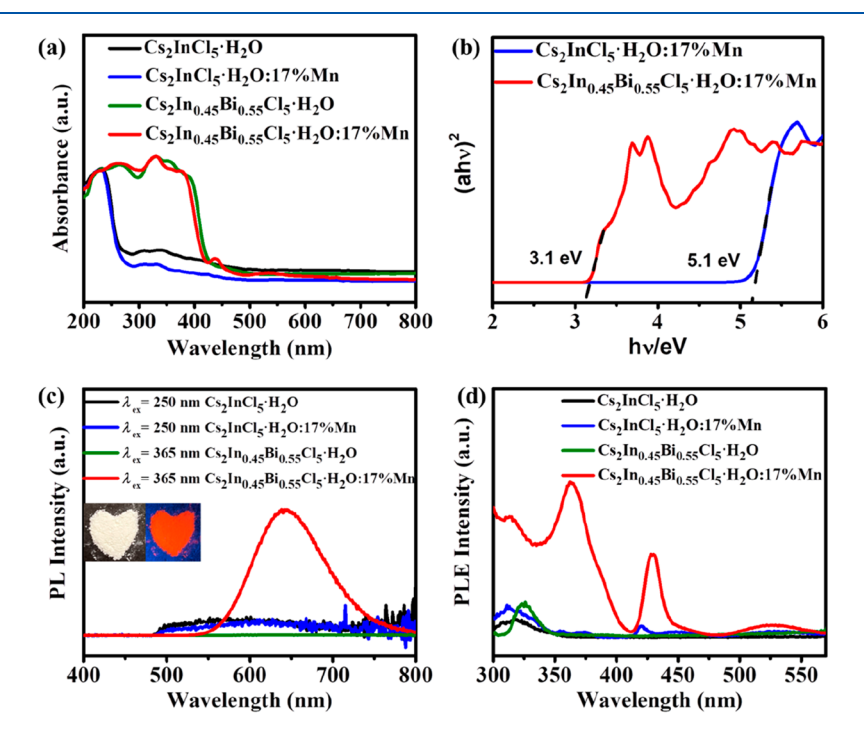


Figure 4. (a) UV–vis absorption spectra of the  $Cs_2InCl_5\cdot H_2O:17\%Mn$  and  $Cs_2In_{0.45}Bi_{0.55}Cl_5\cdot H_2O:17\%Mn$  MCs, (b) related Tauc plot, (c) PL (excitation at 365 nm; inset: a photograph of the  $Cs_2In_{0.45}Bi_{0.55}Cl_5\cdot H_2O:17\%Mn$  under natural light (left) and UV light (right) a 365 nm UV lamp), and (d) PLE (monitored at 640 nm, the intensity of the original sample,  $Mn^{2+}$ -doped or  $Bi^{3+}$ -alloyed are magnified by 5 times) spectra of the  $Cs_2InCl_5\cdot H_2O:17\%Mn$ ,  $Cs_2In_{0.45}Bi_{0.55}Cl_5\cdot H_2O:17\%Mn$  MCs.

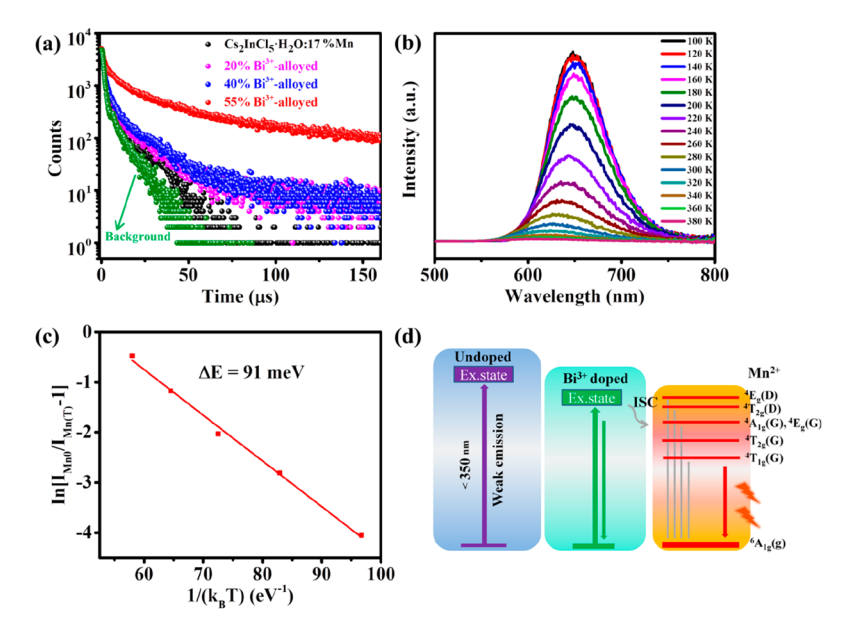


Figure 5. (a) Time-resolved PL decay profiles of different amounts  $\mathrm{Bi}^{3+}$ -incorporated  $\mathrm{Cs_2InCl_5}\cdot\mathrm{H_2O}:17\%\mathrm{Mn}$  MCs (upon excitation at 365 nm). (b) Temperature-dependent PL spectra of  $\mathrm{Cs_2In_{0.45}Bi_{0.55}Cl_5}\cdot\mathrm{H_2O}:17\%\mathrm{Mn}$  MCs. (c) Fitting results of the integrated PL intensity as a function of temperature for  $\mathrm{Cs_2In_{0.45}Bi_{0.55}Cl_5}\cdot\mathrm{H_2O}:17\%\mathrm{Mn}$  MCs. Thermal quenching of PL was fitted using the relation  $I(A) = I_0/[1 + A \exp(-E_a/k_BT)]$ , where  $E_a$  is the thermal activation energy for PL quench,  $I_0$  is the integrated PL intensity at 0 K, and  $k_B$  is the Boltzmann constant. (d) Energy levels and fluorescent mechanism, where ISC represents intersystem crossing.

presence of Mn<sup>2+</sup>, which has also been reported previously.<sup>41–43</sup> The Bi<sup>3+</sup> alloying enhances the PL intensity by 60 times compared to that of Cs<sub>2</sub>InCl<sub>5</sub>·H<sub>2</sub>O:17%Mn. The PL enhancement can be attributed to energy transfer (ET) from Bi<sup>3+</sup> activators to Mn<sup>2+</sup>. We also studied other samples with different Bi/(In + Bi) molar feed ratios; as shown in Figure S3a,b, the PL intensity increases and absorption bands red-shift as the Bi content increases, with the highest PLQY for the Cs<sub>2</sub>In<sub>0.45</sub>Bi<sub>0.55</sub>Cl<sub>5</sub>·H<sub>2</sub>O:17%Mn sample of 1.82%, which is 92 times compared to the unalloyed Cs<sub>2</sub>InCl<sub>5</sub>·H<sub>2</sub>O:17%Mn (Table S2). However, the PLQY of Cs<sub>2</sub>In<sub>0.45</sub>Bi<sub>0.55</sub>Cl<sub>5</sub>· H<sub>2</sub>O:17%Mn is still low, and we speculate that there are two main reasons why PLQY is so low. One is the samples prepared by room-temperature supersaturation recrystallization have many defects, resulting in trap-assisted nonradiative recombination. The other is that Cs<sub>2</sub>InCl<sub>5</sub>·H<sub>2</sub>O is a 0D structure with soft lattices which slows the ET from Bi<sup>3+</sup> activators to Mn<sup>2+</sup> centers. This result is similar to previous reports. 35,44 The samples with different doping amounts of Mn<sup>2+</sup> were further explored. The PL intensity increases with the increase of Mn<sup>2+</sup> (Figure S3c). However, more Mn<sup>2+</sup> will lead to Mn<sup>2+</sup> self-quenching, which will reduce PL intensity. A molar feed ratio of 17% of Mn-doped Cs<sub>2</sub>In<sub>0.45</sub>Bi<sub>0.55</sub>Cl<sub>5</sub>·H<sub>2</sub>O shows the highest PL intensity. As a control experiment, we also use Pb2+ or Sb3+ ions to replace Bi3+ to alloyed Cs2InCl5. H<sub>2</sub>O:Mn. From Figure S4a, Pb<sup>2+</sup> or Sb<sup>3+</sup> ion alloying also shows a higher absorption at 200-400 nm, and the absorption edge red-shifts approximately 200 nm compared to the unalloyed sample. However, the Mn<sup>2+</sup> characteristic absorption peak appears only in the case of Bi<sup>3+</sup> alloying. In Figure S4b, the Pb2+-alloyed sample shows no PL, and the PL intensity of the Sb<sup>3+</sup>-alloyed sample is lower than that of Bi<sup>3+</sup> alloying.

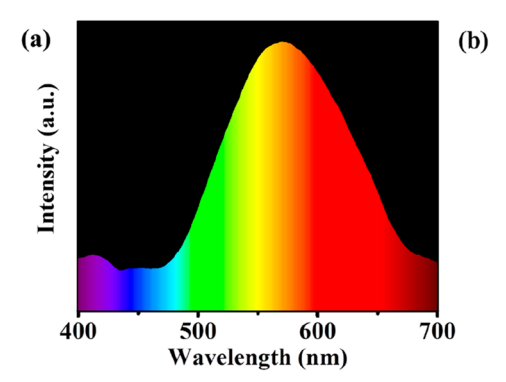
To better establish that the introduction of  $Bi^{3+}$  improves the absorption of light, the PLE spectra of the powder samples were measured as shown in Figure 4d. The pristine  $Cs_2InCl_5$ ·  $H_2O$  and single  $Mn^{2+}$ -doped or  $Bi^{3+}$ -alloyed samples display a

relatively low-intensity response to the weak absorption. However, the PLE intensity is significantly enhanced by the coalloying of Bi<sup>3+</sup> and In<sup>3+</sup>. The maximum excitation peak at about 365 nm is the typical excitation band arising from the Bi<sup>3+</sup> absorption (the spin-orbital-allowed  $^{1}S_{0}-^{3}P_{1}$ ),  $^{45}$  and the peaks at 430 nm are assigned to the  $^{6}A_{1g} \rightarrow ^{4}T_{1g}$  transition of Mn<sup>2+</sup>. The excitation-wavelength-dependent PL and emission-wavelength-dependent PLE spectra were measured. As shown in Figure S5a,b, no significant shift is found in PL spectra when the excitation wavelength increases from 320 to 400 nm. The independence of PL excitation spectra of emission wavelength also confirms that the broad red emission originates from the relaxation of the same excited state.  $^{46}$ 

To help determine the mechanism of Mn<sup>2+</sup>-induced emission, TRPL was measured to understand the effect of Bi<sup>3+</sup> ion alloying on optical properties and exciton dynamics (Figure 5a). The TRPL decay curves of the Bi<sup>3+</sup>-alloyed sample emission can be fitted by double-exponential decay

$$I(t) = A_1 e^{-t/\tau_1} + A_2 e^{-t/\tau_2}$$
(1)

where  $A_1$  and  $A_2$  are amplitudes and  $\tau_1$  and  $\tau_2$  represent fast and slow decay components, respectively. The average lifetime is calculated using  $\tau_{\text{avg}} = (A_1 \tau_1^2 + A_2 \tau_2^2)/(A_1 \tau_1 + A_2 \tau_2)$ . The lifetime distribution statistics are shown in Table S3. The fitting results show two components: (i) the fast component is assigned to trap-assisted nonradiative recombination, and (ii) the slow component is attributed to the  ${}^4T_{1g} \rightarrow {}^6A_{1g}$  radiation recombination of Mn<sup>2+</sup>. The fast PL decay times increased from 1.5  $\mu$ s for single Mn<sup>2+</sup>-doped MCs to 2.2  $\mu$ s for Cs<sub>2</sub>In<sub>0.45</sub>Bi<sub>0.55</sub>Cl<sub>5</sub>·H<sub>2</sub>O:17%Mn MCs. The slow decay times increased from 15.8  $\mu$ s for single Mn<sup>2+</sup>-doped MCs to 25.2  $\mu$ s for Cs<sub>2</sub>In<sub>0.45</sub>Bi<sub>0.55</sub>Cl<sub>5</sub>·H<sub>2</sub>O:17%Mn MCs. With rising Bi<sup>3+</sup> concentration, the average lifetime of Mn2+ increased from 6.0  $\mu$ s for single Mn<sup>2+</sup>-doped MCs to 21.0  $\mu$ s for Cs<sub>2</sub>In<sub>0.45</sub>Bi<sub>0.55</sub>Cl<sub>5</sub>·H<sub>2</sub>O:17%Mn MCs and has a variation tendency similar to its emission intensity. The prolonged



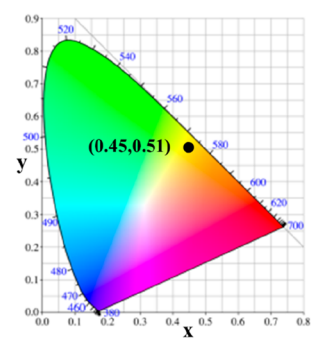


Figure 6. (a) PL spectrum of the fabricated LED device (using a 365 nm near-UV chip) based on  $Cs_2In_{0.45}Bi_{0.55}Cl_5 \cdot H_2O:17\%Mn$  powder under driving currents of 420 mA. (b) Chromaticity coordinates (black dot) in the CIE 1931 system.

 $Mn^{2+}$  lifetime could be assigned to the ET from the  $[BiCl_6]^{3-}$  unit, which acts as UV light absorber and exciton donor, to  $[MnCl_6]^{4-}$  and results in the enhanced concentration of electrons in the excited state, improving the  $^4T_{1g}-^6A_{1g}$  transition process in  $Mn^{2+}.^{38,47-51}$ 

To further reveal the mechanism behind the observed PL, the temperature-dependent PL spectra of  $Cs_2In_{0.45}Bi_{0.55}Cl_5$ ·  $H_2O:17\%Mn$  were measured, as shown in Figure 5b. From 100 to 360 K, the PL peak intensity decreases with increasing temperature, indicating that  $Cs_2InCl_5$ · $H_2O$  is sensitive to temperature. The emission peaks show a blue-shift trend with increasing temperature, which is due to the increase of the bandgap of  $^4T_{1g}$ – $^6A_{1g}$  caused by the lattice expansion with the increasing temperature. Moreover, the thermal activation energy  $(E_a)$  required for transferring excitons to  $Mn^{2+}$  can be estimated through the following equation  $^{38,46}$ 

$$I(A) = I_0 / [1 + A \exp(-E_a / k_B T)]$$
 (2)

where  $I_{\rm Mn}(T)$  and  $I_0$  are the integrated PL intensity at T and 0 K, respectively, and  $k_{\rm B}$  is the Boltzmann constant. As shown in Figure 5c, the  $E_{\rm a}$  was calculated to be 91 meV for  ${\rm Cs_2In_{0.45}Bi_{0.55}Cl_5\cdot H_2O:17\%Mn}$ , which is much lower than the  $E_{\rm a}$  of exciton-to-Mn<sup>2+</sup> transfer in Mn<sup>2+</sup>-doped CsPbCl<sub>3</sub> nanocrystal (~314 meV), indicating that  $[{\rm BiX_6}]^{3-}$  transferred to Mn<sup>2+</sup> via ISC process is readily spontaneous.

Based on the above analysis, the major photophysical processes involved in the  $Bi^{3+}$ -alloyed  $Cs_2InCl_5\cdot H_2O:17\%Mn$  MCs are explained below and illustrated in Figure 5d. The pristine  $Cs_2InCl_5\cdot H_2O$  and  $Cs_2InCl_5\cdot H_2O:17\%Mn$  show very weak PL at a different excitation wavelength due to the parity transition of  $In^{3+}.^{25}$  Upon  $Bi^{3+}$  alloying, the  $[BiCl_6]^{3-}$  octahedron is formed and serves as an excellent light absorber to produce photoexcitons, which can be immediately transferred to the  $[MnCl_6]^{4-}$  octahedron via intersystem crossing (ISC). The accepted excitons can effectively increase the exciton density in  $^4T_{1g}$ , promoting the transition process of  $^4T_{1g} \rightarrow ^6A_{1g}$  of  $Mn^{2+}$  and resulting in the PL intensity enhancement, similar to a previous report.  $^{38}$ 

The coupling effect between electrons and phonons can usually be obtained by fitting the relationship between FWHM and temperature by eq 3:<sup>52</sup>

$$FWHM = 2.36\sqrt{S} \,\hbar\omega \sqrt{\coth\left(\frac{\hbar\omega}{2kT}\right)}$$
(3)

The Huang–Rhys factor (S) and phonon frequency ( $\hbar\omega_{\rm phonon}$ ) are calculated to be 22.68 and 23.57 meV, respectively.

Compared with other luminescent materials, the Huang–Rhys factor of  $\mathrm{Bi^{3^{+}}}$ -alloyed  $\mathrm{Cs_2InCl_5}$ · $\mathrm{H_2O:17\%Mn}$  is relatively high, indicating strong electron–phonon coupling of  $\mathrm{Bi^{3^{+}}}$  in  $\mathrm{Cs_2InCl_5}$ · $\mathrm{H_2O:17\%Mn}$  MCs.

The relative PL intensity was conducted as a function of exposure time in the water. As shown in Figure S6a, the relative PL intensity of Cs<sub>2</sub>In<sub>0.45</sub>Bi<sub>0.55</sub>Cl<sub>5</sub>·H<sub>2</sub>O:17%Mn MCs remains at 61.5% after 1 h in the water. As shown in Figure S6b, the XRD patterns of Cs<sub>2</sub>In<sub>0.45</sub>Bi<sub>0.55</sub>Cl<sub>5</sub>·H<sub>2</sub>O:17%Mn MCs which were stored in air for 80 days were conducted, and there were no obvious impurities or phase transitions compared to the freshly prepared sample. The results show that the Cs<sub>2</sub>In<sub>0.45</sub>Bi<sub>0.55</sub>Cl<sub>5</sub>·H<sub>2</sub>O:17%Mn powder MC sample has stability against water and moisture.

The prepared phosphor powders were studied as color conversion materials to fabricate LEDs. The Cs<sub>2</sub>In<sub>0.45</sub>Bi<sub>0.55</sub>Cl<sub>5</sub>· H<sub>2</sub>O:17%Mn red emitting powder was mixed with curable resin and coated on a commercially available 365 nm GaN LED chip. Figure 6a displays the PL spectra of the LED device under a current of 420 mA. The chromaticity coordinate in the CIE 1931 system is drawn in Figure 6b. The LED device exhibits bright yellow emission with coordinates of (0.46, 0.52), corresponding to a color-rendering index of 56. In addition, the correlated color temperature (CCT) is 3508 K, in line with the national lighting standards, and the LED device exhibits up to 88.5% color purity. The emission from the device is considerably blue-shifted. We speculate that the reason for the considerable blue-shift is caused by the high temperature generated by the large amount of Joule heat generated during device testing under 420 mA driven current, which led to the increase of the bandgap of  ${}^4T_{1g} - {}^6A_{1g}$  caused by the lattice expansion with the increasing temperature. 53 Fig-Figure S7 shows the PL spectra ( $\lambda_{ex} = 365$  nm) of the fabricated device at drive currents by raising the drive current from 300 to 420 mA. It can be observed that the PL band shape exhibits no distinct change. From 320 to 420 mA, the intensity of the emission grows steadily and linearly, showing that the built LED operates effectively at larger driving currents. These results indicate that inorganic lead-free 0D perovskites have certain development potential in solid-state lighting.

#### CONCLUSION

In summary, a lead-free all-inorganic heterometallic luminescent perovskite Cs<sub>2</sub>In<sub>0.45</sub>Bi<sub>0.55</sub>Cl<sub>5</sub>·H<sub>2</sub>O:17%Mn was prepared by a facile precipitation method at room temperature in hydrochloric acid. With Bi<sup>3+</sup> alloying, the absorption band edge

shifts to longer wavelengths, and a 60-fold enhancement is achieved in PL intensity for  $Cs_2In_{0.45}Bi_{0.55}Cl_5 \cdot H_2O:17\%Mn$  compared to the  $Cs_2InCl_5 \cdot H_2O:17\%Mn$ . The PL intensity enhancement was attributed to the formation of a  $[BiCl_6]^{3-}$  octahedron upon  $Bi^{3+}$  alloying and the synergistic effect in the  $Cs_2InCl_5 \cdot H_2O:17\%Mn$ , where the  $[BiCl_6]^{3-}$  unit acts as UV light absorber and exciton donor, which can be subsequently transferred to the  $[MnCl_6]^{4-}$  unit via ISC and promote the transition process of  $^4T_{1g} \rightarrow ^6A_{1g}$  of  $Mn^{2+}$ . In addition, the asprepared  $Cs_2In_{0.45}Bi_{0.55}Cl_5 \cdot H_2O:17\%Mn$  was studied as a color conversion material with a commercial 365 nm GaN LED chip for yellow light emission. This work provides deep insights into the excited-state dynamics of  $Bi^{3+}$  and  $Mn^{2+}$  in  $Cs_2InCl_5 \cdot H_2O$ , thus laying a foundation for the future design of efficient redemitting lead-free perovskite-derivative metal halides via  $ns^2$  metal and  $Mn^{2+}$  ion alloying and doping.

# ASSOCIATED CONTENT

# Supporting Information

The Supporting Information is available free of charge at https://pubs.acs.org/doi/10.1021/acs.jpcc.2c08308.

Schematic preparation process, XRD patterns, PL, absorbance and PLQY of  $Cs_2In_{1-x}Bi_xCl_5\cdot H_2O:17\%Mn$ , SEM images, stability, ICP-OES, the parameter for TRPL profiles of  $Cs_2InCl_5\cdot H_2O:17\%Mn$  and  $Cs_2In_{0.45}Bi_{0.55}Cl_5\cdot H_2O:17\%Mn$ , PL and absorbance of Pb<sup>2+</sup>, Sb<sup>3+</sup>, Bi<sup>3+</sup>-alloyed  $Cs_2InCl_5\cdot H_2O:17\%Mn$ , excitation wavelength-dependent PL spectra and emission wavelength-dependent PLE spectra of  $Cs_2In_{0.45}Bi_{0.55}Cl_5\cdot H_2O:17\%Mn$  (PDF)

# AUTHOR INFORMATION

## **Corresponding Author**

Qi Pang — School of Chemistry and Chemical Engineering/ Guangxi Key Laboratory of Electrochemical Energy Materials, Guangxi University, Nanning 530004 Guangxi, People's Republic of China; orcid.org/0000-0002-5190-1250; Email: pqigx@163.com

## **Authors**

Liang Jing — School of Chemistry and Chemical Engineering/ Guangxi Key Laboratory of Electrochemical Energy Materials, Guangxi University, Nanning 530004 Guangxi, People's Republic of China

Qingmei Cen – School of Chemistry and Chemical Engineering/Guangxi Key Laboratory of Electrochemical Energy Materials, Guangxi University, Nanning 530004 Guangxi, People's Republic of China

Jin Zhong Zhang — Department of Chemistry and Biochemistry, University of California, Santa Cruz, Santa Cruz, California 95064, United States; ⊚ orcid.org/0000-0003-3437-912X

Complete contact information is available at: https://pubs.acs.org/10.1021/acs.jpcc.2c08308

#### Notes

The authors declare no competing financial interest.

## ACKNOWLEDGMENTS

This work was supported by the National Natural Science Foundation of China (Grant 21965003). J.Z.Z. acknowledges the US NSF (CHE-1904547) for financial support.

#### REFERENCES

- (1) Shamsi, J.; Urban, A. S.; Imran, M.; De Trizio, L.; Manna, L. Metal Halide Perovskite Nanocrystals: Synthesis, Post-Synthesis Modifications, and Their Optical Properties. *Chem. Rev.* **2019**, *119*, 3296–3348.
- (2) Wang, Y.; Jia, C.; Fan, Z.; Lin, Z.; Lee, S. J.; Atallah, T. L.; Caram, J. R.; Huang, Y.; Duan, X. Large-Area Synthesis and Patterning of All-Inorganic Lead Halide Perovskite Thin Films and Heterostructures. *Nano Lett.* **2021**, *21*, 1454–1460.
- (3) Dutta, A.; Vyas, M. K.; Bhowmik, K.; Ota, J.; Hait, S. K.; Chandrasekaran, K.; Saxena, D.; Ramakumar, S. S. V. Phase Sensitivity of All-Inorganic Lead Halide Perovskite Nanocrystals. *Mater. Lett.* **2022**, *4*, 2106–2124.
- (4) Protesescu, L.; Yakunin, S.; Bodnarchuk, M. I.; Krieg, F.; Caputo, R.; Hendon, C. H.; Yang, R. X.; Walsh, A.; Kovalenko, M. V. Nanocrystals of Cesium Lead Halide Perovskites (CsPbX<sub>3</sub>, X = Cl, Br, and I): Novel Optoelectronic Materials Showing Bright Emission with Wide Color Gamut. *Nano Lett.* **2015**, *15*, 3692–3696.
- (5) Swift, M. W.; Lyons, J. L. First-Principles Survey of Acceptor Dopants for P-Type Cesium Lead Bromide. *J. Phys. Chem. C* **2022**, 126, 12294–12300.
- (6) Román-Vázquez, M.; Vidyasagar, C. C.; Muñoz-Flores, B. M.; Jiménez-Pérez, V. M. Recent Advances on Synthesis and Applications of Lead-and Tin-Free Perovskites. *J. Alloys Compd.* **2020**, 835, 155112
- (7) Lyu, M.; Yun, J. H.; Chen, P.; Hao, M.; Wang, L. Addressing Toxicity of Lead: Progress and Applications of Low-Toxic Metal Halide Perovskites and Their Derivatives. *Adv. Energy Mater.* **2017**, *7*, 1602512
- (8) Li, W.; Liu, Q.; Zhang, Y.; Li, C.; He, Z.; Choy, W. C. H.; Low, P. J.; Sonar, P.; Kyaw, A. K. K. Biodegradable Materials and Green Processing for Green Electronics. *Adv. Mater.* **2020**, 32, 2001591.
- (9) He, S.; Fang, S.; Han, T.; Lang, T.; Cai, M.; You, H.; Peng, L.; Cao, S.; Liu, B.; Qiang, Q.; et al. Spectral Red-Shift of  $Cs_4Mn-(Bi_{1-X}In_x)_2Cl_{12}$  Layered Double Perovskite by Adjusting the Microstructure of the  $[MnCl_6]^{4-}$  Octahedron. *J. Phys. Chem. C* **2021**, *125*, 16938–16945.
- (10) Shi, H.; Han, D.; Chen, S.; Du, M.-H. Impact of Metal ns<sup>2</sup> Lone Pair on Luminescence Quantum Efficiency in Low-Dimensional Halide Perovskites. *Phys. Rev. Mater.* **2019**, *3*, No. 034604.
- (11) McCall, K. M.; Morad, V.; Benin, B. M.; Kovalenko, M. V. Efficient Lone-Pair-Driven Luminescence: Structure-Property Relationships in Emissive 5s<sup>2</sup> Metal Halides. *Mater. Lett.* **2020**, *2*, 1218–1232
- (12) Arfin, H.; Kshirsagar, A. S.; Kaur, J.; Mondal, B.; Xia, Z.; Chakraborty, S.; Nag, A. ns<sup>2</sup> Electron (Bi<sup>3+</sup> and Sb<sup>3+</sup>) Doping in Lead-Free Metal Halide Perovskite Derivatives. *Chem. Mater.* **2020**, *32*, 10255–10267.
- (13) Zhou, G.; Su, B.; Huang, J.; Zhang, Q.; Xia, Z. Broad-Band Emission in Metal Halide Perovskites: Mechanism, Materials, and Applications. *Mater. Sci. Eng. R Rep.* **2020**, *141*, 100548.
- (14) Tan, Z.; Li, J.; Zhang, C.; Li, Z.; Hu, Q.; Xiao, Z.; Kamiya, T.; Hosono, H.; Niu, G.; Lifshitz, E.; Cheng, Y.; Tang, J. Highly Efficient Blue-Emitting Bi-Doped Cs<sub>2</sub>SnCl<sub>6</sub> Perovskite Variant: Photoluminescence Induced by Impurity Doping. *Adv. Funct. Mater.* **2018**, 28, 18011.
- (15) Zhou, B.; Liu, Z.; Fang, S.; Zhong, H.; Tian, B.; Wang, Y.; Li, H.; Hu, H.; Shi, Y. Efficient White Photoluminescence from Self-Trapped Excitons in Sb<sup>3+</sup>/Bi<sup>3+</sup>-Codoped Cs<sub>2</sub>NaInCl<sub>6</sub> Double Perovskites with Tunable Dual-Emission. *ACS Energy Lett.* **2021**, *6*, 3343–3351.
- (16) Wang, C.; Mao, X.; Wang, Z.; Xu, X.; Guo, W.; Zhang, R. Synthesis and Exciton Dynamics of a One-Dimensional Organic Copper Halide Perovskite. *J. Phys. Chem. C* **2022**, *126*, 4959–4964.
- (17) Han, P.; Zhou, W.; Zheng, D.; Zhang, X.; Li, C.; Kong, Q.; Yang, S.; Lu, R.; Han, K. Lead-Free All-Inorganic Indium Chloride Perovskite Variant Nanocrystals for Efficient Luminescence. *Adv. Opt. Mater.* **2022**, *10*, 2101344.

- (18) Han, P.; Luo, C.; Yang, S.; Yang, Y.; Deng, W.; Han, K. All-Inorganic Lead-Free 0d Perovskites by a Doping Strategy to Achieve a PLQY Boost from < 2% to 90. *Angew. Chem., Int. Ed.* **2020**, 59, 12709–12713.
- (19) Majher, J. D.; Gray, M. B.; Liu, T.; Holzapfel, N. P.; Woodward, P. M. Rb<sub>3</sub>InCl<sub>6</sub>: A Monoclinic Double Perovskite Derivative with Bright Sb<sup>3+</sup>-Activated Photoluminescence. *Inorg. Chem.* **2020**, *59*, 14478–14485.
- (20) Shao, H.; Wu, X.; Zhu, J.; Xu, W.; Xu, L.; Dong, B.; Hu, J.; Dong, B.; Bai, X.; Cui, H.; et al. Mn<sup>2+</sup> Ions Doped Lead-Free Zero-Dimensional K<sub>3</sub>SbCl<sub>6</sub> Perovskite Nanocrystals Towards White Light Emitting Diodes. *Chem. Eng. J.* **2021**, *413*, 127415.
- (21) Li, M.; Xia, Z. Recent Progress of Zero-Dimensional Luminescent Metal Halides. *Chem. Soc. Rev.* **2021**, *50*, 2626–2662.
- (22) Jing, Y.; Liu, Y.; Jiang, X.; Molokeev, M. S.; Lin, Z.; Xia, Z. Sb<sup>3+</sup> Dopant and Halogen Substitution Triggered Highly Efficient and Tunable Emission in Lead-Free Metal Halide Single Crystals. *Chem. Mater.* **2020**, 32, 5327–5334.
- (23) Liu, X.; Xu, X.; Li, B.; Liang, Y.; Li, Q.; Jiang, H.; Xu, D. Antimony-Doping Induced Highly Efficient Warm-White Emission in Indium-Based Zero-Dimensional Perovskites. CCS 2020, 2, 216–224.
- (24) Zhu, D.; Zaffalon, M. L.; Zito, J.; Cova, F.; Meinardi, F.; De Trizio, L.; Infante, I.; Brovelli, S.; Manna, L. Sb-Doped Metal Halide Nanocrystals: A 0D Versus 3D Comparison. *ACS Energy Lett.* **2021**, *6*, 2283–2292.
- (25) Wei, J.; Luo, J.; Liao, J.; Ou, W.; Kuang, D. Te<sup>4+</sup>-Doped Cs<sub>2</sub>InCl<sub>5</sub>·H<sub>2</sub>O Single Crystals for Remote Optical Thermometry. *Sci. China Mater.* **2022**, *65*, 764–772.
- (26) Gong, Z.; Zheng, W.; Huang, P.; Cheng, X.; Zhang, W.; Zhang, M.; Han, S.; Chen, X. Highly Efficient Sb<sup>3+</sup> Emitters in 0D Cesium Indium Chloride Nanocrystals with Switchable Photoluminescence through Water-Triggered Structural Transformation. *Nano Today* **2022**, *44*, 101460.
- (27) Rajamanickam, N.; Chowdhury, T. H.; Isogami, S.; Islam, A. Magnetic Properties in CH<sub>3</sub>NH<sub>3</sub>PbI<sub>3</sub> Perovskite Thin Films by Mn Doping. *J. Phys. Chem. C* **2021**, *125*, 20104–20112.
- (28) Mir, W. J.; Jagadeeswararao, M.; Das, S.; Nag, A. Colloidal Mn-Doped Cesium Lead Halide Perovskite Nanoplatelets. *ACS Energy Lett.* **2017**, *2*, 537–543.
- (29) Zhou, S.; Zhu, Y.; Zhong, J.; Tian, F.; Huang, H.; Chen, J.; Chen, D. Chlorine-Additive-Promoted Incorporation of Mn<sup>2+</sup> Dopants into CsPbCl<sub>3</sub> Perovskite Nanocrystals. *NANOSCALE* **2019**, *11*, 12465–12470.
- (30) Forde, A.; Thomas, S. A.; Petersen, R. J.; Brown, S. L.; Kilin, D. S.; Hobbie, E. K. Size-Dependent Doping Synergy and Dual-Color Emission in CsPb<sub>1-X</sub>Mn<sub>x</sub>Cl<sub>3</sub> Nanocrystals. *J. Phys. Chem. C* **2021**, *125*, 18849–18856.
- (31) Guria, A. K.; Dutta, S. K.; Adhikari, S. D.; Pradhan, N. Doping Mn<sup>2+</sup> in Lead Halide Perovskite Nanocrystals: Successes and Challenges. *ACS Energy Lett.* **2017**, *2*, 1014–1021.
- (32) Das Adhikari, S.; Guria, A. K.; Pradhan, N. Insights of Doping and the Photoluminescence Properties of Mn-Doped Perovskite Nanocrystals. *J. Phys. Chem. Lett.* **2019**, *10*, 2250–2257.
- (33) Du, P.; Cai, P.; Li, W.; Luo, L.; Hou, Y.; Liu, Z. Ratiometric Optical Thermometer Based on the Use of Manganese(II)-Doped Cs<sub>3</sub>Cu<sub>2</sub>I<sub>5</sub> Thermochromic and Fluorescent Halides. *Microchimica Acta.* **2019**, *186*, 730.
- (34) Li, X.; Chen, J.; Yang, D.; Chen, X.; Geng, D.; Jiang, L.; Wu, Y.; Meng, C.; Zeng, H.  $Mn^{2+}$  Induced Significant Improvement and Robust Stability of Radioluminescence in  $Cs_3Cu_2I_5$  for High-Performance Nuclear Battery. *Nat. Commun.* **2021**, *12*, 3879.
- (35) Yan, J.; Zhang, S.; Wei, Q.; Cao, S.; Zhao, J.; Zou, B.; Zeng, R. Stoichiometry-Controlled Phase Engineering of Cesium Bismuth Halides and Reversible Structure Switch. *Adv. Opt. Mater.* **2022**, *10*, 2101406
- (36) Wang, X.; Ali, N.; Bi, G.; Wang, Y.; Shen, Q.; Rahimi-Iman, A.; Wu, H. Lead-Free Antimony Halide Perovskite with Heterovalent Mn<sup>2+</sup> Doping. *Inorg. Chem.* **2020**, *59*, 15289–15294.

- (37) De Siena, M. C.; Sommer, D. E.; Creutz, S. E.; Dunham, S. T.; Gamelin, D. R. Spinodal Decomposition During Anion Exchange in Colloidal  $Mn^{2+}$ -Doped  $CsPbX_3$  (X = Cl, Br) Perovskite Nanocrystals. *Chem. Mater.* **2019**, *31*, 7711–7722.
- (38) Wei, J.; Liao, J.; Wang, X.; Zhou, L.; Jiang, Y.; Kuang, D. All-Inorganic Lead-Free Heterometallic Cs<sub>4</sub>MnBi<sub>2</sub>Cl<sub>12</sub> Perovskite Single Crystal with Highly Efficient Orange Emission. *Matter* **2020**, *3*, 892–903.
- (39) Sun, Y.; Fernández-Carrión, A. J.; Liu, Y.; Yin, C.; Ming, X.; Liu, B.-M.; Wang, J.; Fu, H.; Kuang, X.; Xing, X. Bismuth-Based Halide Double Perovskite Cs<sub>2</sub>LiBiCl<sub>6</sub>: Crystal Structure, Luminescence, and Stability. *Chem. Mater.* **2021**, 33, 5905–5916.
- (40) Li, H. H.; Wang, C. F.; Wu, Y. X.; Jiang, F.; Shi, C.; Ye, H. Y.; Zhang, Y. Halogen Substitution Regulates the Phase Transition Temperature and Band Gap of Semiconductor Compounds. *ChemComm* **2020**, *56*, 1697–1700.
- (41) K, N. N.; Nag, A. Synthesis and Luminescence of Mn-Doped Cs<sub>2</sub>AgInCl<sub>6</sub> Double Perovskites. *Chem. Commun.* **2018**, *54*, 5205–5208.
- (42) Locardi, F.; Cirignano, M.; Baranov, D.; Dang, Z.; Prato, M.; Drago, F.; Ferretti, M.; Pinchetti, V.; Fanciulli, M.; Brovelli, S.; et al. Colloidal Synthesis of Double Perovskite Cs<sub>2</sub>AgInCl<sub>6</sub> and Mn-Doped Cs<sub>2</sub>AgInCl<sub>6</sub> Nanocrystals. *J. Am. Chem. Soc.* **2018**, *140*, 12989–12995.
- (43) Wu, W.; Cong, W. Y.; Guan, C.; Sun, H.; Yin, R.; Yu, G.; Lu, Y. B. Investigation of the Mn Dopant-Enhanced Photoluminescence Performance of Lead-Free Cs<sub>2</sub>AgInCl<sub>6</sub> Double Perovskite Crystals. *Phys. Chem. Chem.* **2020**, 22, 1815–1819.
- (44) Liu, M.; Ali-Loytty, H.; Hiltunen, A.; Sarlin, E.; Qudsia, S.; Smatt, J. H.; Valden, M.; Vivo, P. Manganese Doping Promotes the Synthesis of Bismuth-Based Perovskite Nanocrystals While Tuning Their Band Structures. *Small* **2021**, *17*, e2100101.
- (45) Zhang, W.; Zheng, W.; Li, L.; Huang, P.; Gong, Z.; Zhou, Z.; Sun, J.; Yu, Y.; Chen, X. Dual-Band-Tunable White-Light Emission from Bi<sup>3+</sup>/Te<sup>4+</sup> Emitters in Perovskite-Derivative Cs<sub>2</sub>SnCl<sub>6</sub> Microcrystals. *Angew. Chem., Int. Ed.* **2022**, *61*, 202116085.
- (46) Meng, Q.; Zhou, L.; Pang, Q.; He, X.; Wei, T.; Zhang, J. Z. Enhanced Photoluminescence of All-Inorganic Manganese Halide Perovskite-Analogue Nanocrystals by Lead Ion Incorporation. *J. Phys. Chem. Lett.* **2021**, *12*, 10204–10211.
- (47) Zhou, W.; Fan, J.; Luo, J.; Wu, J.; Zhang, R.; Zhang, J.; Pang, Q.; Zhou, L.; Zhang, T.; Zhang, X. Novel High-Saturated Red-Emitting Phosphor  $Sr_9(Mg_{0.5}Mn_{0.5})K(PO_4)_7$ : Eu<sup>2+</sup> with Great Quantum Efficiency Enhancement by La<sup>3+</sup> Codoping for White Led Application. *Mater. Today Chem.* **2023**, 27, 101263.
- (48) Zhang, X.; Luo, J.; Sun, Z.; Zhou, W.; Wu, Z. C.; Zhang, J. Ultrahigh-Energy-Transfer Efficiency and Efficient Mn<sup>2+</sup> Red Emission Realized by Structural Confinement in Ca<sub>9</sub>LiMn-(PO<sub>4</sub>)<sub>7</sub>:Eu<sup>2+</sup>,Tb<sup>3+</sup> Phosphor. *Inorg. Chem.* **2020**, *59*, 15050–15060.
- (49) Hu, Y.; Yan, X.; Zhou, L.; Chen, P.; Pang, Q.; Chen, Y. Improved Energy Transfer in Mn-Doped Cs<sub>3</sub>Cu<sub>2</sub>I<sub>5</sub> Microcrystals Induced by Localized Lattice Distortion. *J. Phys. Chem. Lett.* **2022**, *13*, 10786–10792.
- (50) Wai, R. B.; Ramesh, N.; Aiello, C. D.; Raybin, J. G.; Zeltmann, S. E.; Bischak, C. G.; Barnard, E.; Aloni, S.; Ogletree, D. F.; Minor, A. M.; et al. Resolving Enhanced Mn<sup>2+</sup> Luminescence near the Surface of CsPbCl<sub>3</sub> with Time-Resolved Cathodoluminescence Imaging. *J. Phys. Chem. Lett.* **2020**, *11*, 2624–2629.
- (51) Zhong, C. Y.; Li, L.; Chen, Q.; Jiang, K. Z.; Li, F. t.; Liu, Z. Q.; Chen, Y. Enhanced Exciton-to-Mn<sup>2+</sup> Energy Transfer in 3D/0D Cesium-Lead-Chloride Composite Perovskites. *Adv. Opt. Mater.* **2022**, 2202321.
- (52) Wu, D.; Liu, L.; Liang, H.; Duan, H.; Nie, W.; Wang, J.; Peng, J.; Ye, X. LiBAlF<sub>6</sub>: $Cr^{3+}$  (B = Ca, Sr) fluoride phosphors with ultrabroad near-infrared emission for NIR pc-LEDs. *CERAM INT* **2022**, 48, 387–396.
- (53) Zhang, K.; Zhu, N.; Zhang, M.; Wang, L.; Xing, J. Opportunities and Challenges in Perovskite Led Commercialization. *J. Mater. Chem. C* **2021**, *9*, 3795–3799.